HAL
open science

Origin and properties of an unexpected exchange bias of Ta/Ni80Fe20/Ir20Mn80/Ta heterostructure in ultrathin limit: Impact of the oblique deposition and Ta/Ni80Fe20 alloying

A.C. Krohling, H.D. Leite, F. Fettar, E. Mossang, J.-M. Tonnerre, R. Magalhães-Paniago, T.E.P. Bueno, E.C. Passamani, V.P. Nascimento

To cite this version:

A.C. Krohling, H.D. Leite, F. Fettar, E. Mossang, J.-M. Tonnerre, et al.. Origin and properties of an unexpected exchange bias of Ta/Ni80Fe20/Ir20Mn80/Ta heterostructure in ultrathin limit: Impact of the oblique deposition and Ta/Ni80Fe20 alloying. Thin Solid Films, 2022, 746, pp.139115. 10.1016/j.tsf.2022.139115 . hal-03760406

HAL Id: hal-03760406

https://hal.science/hal-03760406v1

Submitted on 25 Aug 2022

HAL is a multi-disciplinary open access archive for the deposit and dissemination of scientific research documents, whether they are published or not. The documents may come from teaching and research institutions in France or abroad, or from public or private research centers.

L'archive ouverte pluridisciplinaire **HAL**, est destinée au dépôt et à la diffusion de documents scientifiques de niveau recherche, publiés ou non, émanant des établissements d'enseignement et de recherche français ou étrangers, des laboratoires publics ou privés.

Thin Solid Films xxx (xxxx) 139115

Contents lists available at ScienceDirect

Thin Solid Films

journal homepage: www.elsevier.com/locate/tsf

Origin and properties of an unexpected exchange bias of $Ta/Ni_{80}Fe_{20}/Ir_{20}Mn_{80}/Ta$ heterostructures in ultrathin limit: Impact of the oblique deposition and $Ta/Ni_{80}Fe_{20}$ alloying

A.C. Krohling [a], H.D. Leite [a], F. Fettar [b], E. Mossang [b], J.M. Tonnerre [b, c], R. Magalhães-Paniago [d], T.E.P. Bueno [a], E.C. Passamani [a], V.P. Nascimento [a, *]

[a] Physics Department, Federal University of Espírito Santo, 29075-910 Vitória, Espírito Santo, Brazil
[b] Univ. Grenoble Alpes, CNRS, Grenoble INP, Institut NEEL, F-38000 Grenoble, France
[c] Synchrotron SOLEIL, Saint-Aubin, Boîte Postale 48, 91192 Gif-sur-Yvette Cedex, France
[d] Physics Department, Federal University of Minas Gerais, 30123-970 Belo Horizonte, Minas Gerais, Brazil

ARTICLE INFO

Keywords:
Ultrathin film
Interface
Magnetic anisotropy
Exchange bias
Shadow effect

ABSTRACT

Ultrathin Si(100)/$Ta/Ni_{80}Fe_{20}/Ir_{20}Mn_{80}/Ta$ heterostructure deposited by oblique incidence in a confocal magnetron sputtering exhibits an unexpected exchange bias effect, despite the rotation of the sample holder and absence of external magnetic field during the deposition. Its magnetic loops have anomalous shifts along the field axis, whose features are non-uniform and strongly dependent on the orientation of the applied magnetic field. Structural, magnetic and thermal properties of the heterostructure were investigated using x-ray scattering and magnetic measurements to highlight the role of interfaces between ultrathin films and the related magnetic effects on the setting of the exchange bias. We show that the shadowing effect due to the oblique incidence of the sputtering flux combined to the atomic diffusion at the $Ta/Ni_{80}Fe_{20}$ interface favors the emergence of a uniaxial anisotropy in the ferromagnetic layer formed by a $Ni_{80}Fe_{20}$ sublayer at the top and a NiFeTa alloy at the bottom. The later increases the uniaxial anisotropy constant of the ferromagnet, which was strong enough to impose a well-defined direction for the spontaneous magnetization and, consequently, set the unidirectional anisotropy during the $Ir_{20}Mn_{80}$ layer formation. The thermal processes can reversibly be applied up to 460 K and, for higher temperatures, there were the vanishing of the exchange bias at 600 K and a thickening of the NiFeTa alloy which led to a reduction in the saturation magnetization of the heterostructure. Therefore, our findings suggest that the role of the interfacial NiFeTa alloy is only revealed in the ultrathin dimension and is imperceptible in thicker samples.

I. Introduction

Magnetic heterostructures involved in the development of spintronics and magnetic storage media have been studied extensively over the last four decades. [1–3]. Within this vast research topic, it has been found that the investigation of the magnetic properties of multilayers can become very complicated by the combined effects from different magnetic anisotropy sources [4, 5]. The *magnetocrystalline anisotropy* (K_{MA}) results from the electric interaction between the non-spherical charge orbital, responsible for the orbital magnetic moment of the atom, and the crystal field created by the ions of the crystalline lattice. It favors the alignment of magnetization in specific directions of the crystal lattice due to the spin-orbit coupling [6,7]. Another important anisotropy is the *shape anisotropy* (K_{SH}), which depends on the sample geometry. It tends to align the magnetic moments in the direction of the longest sample dimension (reduction of magnetostatic energy of the sample). For uniform thin films, the K_{SH} energy is simply given by:

$$K_{SH} = -\frac{\mu_0}{2} M_S^2 sin^2 \beta, \tag{1}$$

where M_S is the saturation magnetization of the ferromagnet and ß is the angle between the orientation of $\boldsymbol{M_S}$ and the normal to the sample plane. Therefore, when the K_{SH} term dominates the magnetic energy of the system, the magnetic moments lie in the film plane ($\beta = 90^0$). However, in case of ultrathin magnetic films (few monolayers of Co or Fe for instance), when the magnetic energy associated with the orbital contri-

* Corresponding author at: Avenida Fernando Ferrari, 514, Campus de Goiabeiras, 29075-910 – Vitória – ES – Brazil.
E-mail address: valberpn@hotmail.com (V.P. Nascimento).

https://doi.org/10.1016/j.tsf.2022.139115
Received 28 July 2021; Received in revised form 23 December 2021; Accepted 27 January 2022
0040-6090/© 2021

UNCORRECTED PROOF

Note: Low-resolution images were used to create this PDF. The original images will be used in the final composition.

bution overcomes K_{SH}, the system may have a *perpendicular magnetic anisotropy* (K_P) that aligns the total magnetic moment perpendicularly to the sample plane ($\beta = 0^0$) [8, 9]. Moreover, changes in the morphology of the samples, like columnar growth, elongated grains, sculptured thin films and step bunching vicinal structures (induced by the deposition methods) can also alter the shape of the samples, resulting in an addition of new energy terms to the K_{SH} expression, besides the ordinary term [see Eq. (1)] [10]. Other sources of anisotropies can contribute to the *magnetic anisotropy* of a ferromagnetic layer (K_{eff}^{FM}), among them, strain, surface, magnetoelastic and magnetostriction [11, 12]. In addition, considering a magnetically coupled ferromagnetic (FM)/antiferromagnetic (AF) bilayer system, a *unidirectional anisotropy* (K_{EB}) may emerge at the interface due to the exchange bias effect (E_B), which is characterized by a shift of the magnetic hysteresis loop along the magnetic field axis often denoted by exchange bias field (H_{EB}) [13]. Generally, E_B can be tuned in the FM/AF system by either field cooling (FC) (temperature effects) or by depositing the system under an external applied magnetic field (H). In case of the FC protocol, ideally the temperature setting is between the Curie temperature (T_C) of the FM and the Néel temperature (T_N) of the AF layer. In principle, E_B is generally induced by FC protocol from temperatures near below T_N [14]. However, E_B may also emerge even in the absence of an applied deposition field, as already observed in as-prepared systems where there is a preferentially oriented spontaneous FM magnetization that favors the exchange bias at the FM/AF interface [15, 16]. Thus, independent on how the exchange bias was set (stimulated by an external field or not), it is possible to consider that E_B is always set by the FM magnetization. In addition, E_B is also strongly influenced by structural and chemical disorder parameters of the FM/AF interface, like roughness and atomic diffusion [17–19]. Furthermore, the K_{eff}^{FM} axis can be redirected when an AF material is magnetically coupled, and its direction can differ from the K_{EB} axis due to the competition between these two anisotropies, revealing an unusual picture of the exchange bias phenomena [4, 5]. In addition, the temperature where the E_B effect vanishes is called blocking temperature (T_B). Thus, depending on the types of anisotropy present in the system and the direction of the applied field during the measurement, the shape of hysteresis loops may be distorted or take on anomalous forms, which complicates the magnetic analysis.

In previous work [20], it has been shown that the Cu (Ta) buffer layer induced a low (high) degree of [111] fiber-texture in the Si(100)/Cu or Ta(10 nm)/$Ni_{80}Fe_{20}$(20 nm)/$Ir_{20}Mn_{80}$(4–15 nm)/Co(10 nm)/Ta or Cu(10 nm) deposited by oblique incidence in a confocal magnetron sputtering with the sample holder spinning at 0.5 Hz. The samples with high degree of [111] texture (with Ta buffer) presented a strong planar magnetic anisotropy, opposite to what happened to the samples with Cu. In addition, the degree of [111] texture also influenced the E_B and the interlayer magnetic coupling. There is no doubt that the buffer materials (Cu and Ta) which induced different degrees of [111] texture in the heterostructures influenced the magnetic anisotropy of this system [20]. However, it is important to point out that the crystalline texture is not the physical origin of the planar magnetic anisotropy. Thereby, extreme magnetic softness has been reported for Py films grown by normal incidence sputtering on Ta buffers, an effect associated with the induction of a strong [111] crystalline texture, since the magnetocrystalline anisotropy energy is isotropic in the (111) plane, i. e., K_{MA} (111) ≈ 0, where, the higher is the degree of [111] texture, the softer is the Py layer [21, 22]. Furthermore, in-plane K_U was observed in $[Cu/Py]_n$ multilayers sputtered on 4° tilt cut Si(111), however, it has been not detected for standard Si(111) [23], suggesting the planar anisotropy was induced by the 4° tilt cut Si(111) substrate slope related to the sample holder that causes an oblique incidence on the sample surface. Later on, it has been demonstrated that the in-plane magnetic anisotropy has the form of a uniaxial anisotropy (K_U) in magnetic multilayers with Cu buffer layer (static sample holder) or Ta buffer layer (static or spinning sample holder) deposited by oblique incidence in a confocal magnetron sputtering system [16, 24-25]. The presence of the K_U energy, expressed as the form:

$$K_U = K_1 sin^2\omega, \tag{2}$$

in these films is generally attributed to the elongated grains (shape anisotropy) formed by the shadowing effect due to the oblique incidence of the sputtering flux [10, 16, 24-26]. The formation of elongated grains due to the shadow effect that appears on thin films deposited by oblique incidence is well known in the literature and it is described in details in Ref. 10. K_1 is the first order uniaxial anisotropy constant, and ω is the angle between the $\boldsymbol{M}$ vector and the $K_U$easy axis. In this case, K_1>0 and the higher order anisotropy constants can be neglected, because the spontaneous $\boldsymbol{M}$ points to the long length of the elongated grains (symmetry axis) where K_U is minimum [7]. Therefore, when the magnetization is in the sample plane, the K_{SH} energy can be written as [27]:

$$K_{SH} = -\frac{\mu_0}{2}M_S^2 + K_1 sin^2\omega. \tag{3}$$

It should be pointed out that the K_U value is strongly reduced when the sample is centered in a spinning sample holder. However, as already shown for the Si(100/Ta(10 nm)/Co(10 nm)/Ta(5 nm) and Si(100)/Al_2O_3(2 nm)/Co(10 nm)/Al_2O_3(2 nm) stacking, K_U still remains with a non-zero value for spinning velocities up to 0.5 Hz. [24, 26].

In the present work, we turned the attention to the ultrathin dimension and thus, we have investigated the structural, magnetic and thermal properties of the ultrathin Si(100)/Ta(3 nm)/$Ni_{80}Fe_{20}$ (3 nm)/$Ir_{20}Mn_{80}$(8 nm)/Ta(1 nm) heterostructure deposited by confocal magnetron sputtering in a spinning substrate holder. The scenario for ultrathin film (few monolayers stacked) is even more complex. The investigation of the magnetic properties of multilayers, composed of ultrathin and 2D films [28, 29], has emerged as a challenge for researchers basically due to three factors: (i) the small amount of material that requires the use of high sensibility measurement techniques, (ii) the interface effects that exert strong influence on the results (and are hidden in thicker samples) and (iii) the magnetism of ultrathin multilayers, in general, that differs strongly from thick film arrangements. The film thickness, below which the ultrathin limit is defined, can be obtained from anisotropy terms [28–33]. In the case of the $N_{i80}Fe_{20}$ alloy, an ultrathin limit thickness of 5 nm, at room temperature (RT), was calculated using its magnetic anisotropy parameters [34–36].

The $Ni_{80}Fe_{20}/Ir_{20}Mn_{80}$ exchange-biased system has been chosen because it has extensively been studied in the last decades, basically due to its high H_{EB}, high T_C (872 K), T_N (730 K) and T_B (520 to 590 K) temperatures, low H_C fields, thermal and structure stability, field sensitivity and corrosion resistance, which enhance its potential for application in magnetic sensors and spin valve heads [37–42]. Ta has been selected as seed layer because it reinforces the (111) crystalline orientation and favors the growth of films with low roughness values and high (low) H_{EB} (H_C) fields [43–45]. The choices of moderate $t_{Ir20Mn80}$ = 8 nm and thinner $t_{Ni80Fe20}$ = 3 nm guarantee continuous layers and that $t_{Ni80Fe20}$ is below the ultrathin limit [34–36]. An interesting aspect of the use of ultrathin FM layers in exchange biased multilayer structures is the fact that they favor higher H_{EB} due to the inverse proportionality with the ferromagnetic layer thickness (FM), i.e., $H_{EB} \propto 1/t_{FM}$ [13, 43, 46]. In addition, ultrathin $Ni_{80}Fe_{20}$ films have often been indicated to be used in spintronic devices that operate with spin pumping into nonmagnetic normal metals [47, 48], but they are also being used to pump spins into antiferromagnetic $Ir_{20}Mn_{80}$ sinks [49, 50].

Magnetic analysis of the Si(100)/Ta/$Ni_{80}Fe_{20}/Ir_{20}Mn_{80}$/Ta heterostructure detected an unexpected anisotropy ($K_{eff}^{FM/AF}$) characterized by anomalous shifts of the hysteresis loops, the origin of which is described in details. The ultrathin dimension of the $Ni_{80}Fe_{20}$ film (3 nm)

UNCORRECTED PROOF

allowed the detection of an alloy at the Ta/$Ni_{80}Fe_{20}$ interface, the presence of which has an important role to set $K_{eff}^{FM/AF}$ and is essential to elucidate the total magnetic response of the heterostucture. Such an effect is imperceptible in thicker samples. The thermal stability of $K_{eff}^{FM/AF}$ was also investigated from RT to 600 K. An increase of the amount of the NiFeTa alloy at the Ta/$Ni_{80}Fe_{20}$ interface was detected at room temperature after a heat treatment at elevated temperatures (500 K – 600 K). This study reveals important details that can contribute for further applications of the NiFe/IrMn heterostructures in spin valve sensors or spintronic devices.

II. Experimental details

Ta(3 nm)/Py(3 nm)/Ta(3 nm) (Sample A) and Ta(3 nm)/Py (3 nm)/IrMn(8 nm)/Ta(1 nm) (Sample B) ultrathin film multilayers, as wells as thicker samples [Ta (50 nm), Py (50 nm), IrMn (50 nm), Ta (20 nm) and Ta(10 nm)/Py(20 nm)/IrMn(15 nm)/Ta(5 nm)], were deposited onto naturally oxidized Si (100) substrates at RT by DC magnetron sputtering in a confocal AJA-Orion 8 setup (for more details, see Bertelli et al. [24]). Py and IrMn denote, respectively, the permalloy ($Ni_{80}Fe_{20}$) and the $Ir_{20}Mn_{80}$ alloy with the aim of simplifying the notation in the manuscript. Rectangular Si(100) substrates (15 × 10 × 0.5 mm^3) were preliminarily cleaned in a sequential bath of neutral detergent, acetone, isopropyl alcohol and dried with a ionized dry N_2 flux. The substrates were mounted at the center of the water-cooled sample holder (291 K) and inserted in the high vacuum deposition chamber with a pressure of about 2.7 × 10^{-6} Pa. A sputtering working pressure of 2.7 × 10^{-1} Pa of high purity argon gas (5 N) was used to create the plasma. The incident sputtering flux makes an angle of 32° with the normal of the sample. The sample holder spun at 0.5 Hz to favor lateral film homogeneity. DC currents of 304 mA, 300 mA and 210 mA were used to start the plasma of the two-inch Ta, $Ni_{80}Fe_{20}$ and $Ir_{20}Mn_{80}$ at.% high purity (4 N) targets, respectively. Their deposition rates were determined using two steps after applying a pre-sputtering process to clean the target surface. First, the 50 nm thick Ta, Py and IrMn single layers were deposited considering the individual deposition rates measured by a moveable quartz crystal microbalance installed in the sputtering deposition chamber (the microbalance is also used to check the stabilization of the deposition rate). Then, X-ray reflectivity (XRR) measurements were performed on these single layers. We used thick monolayer samples (50 nm) for the thickness calibration in order to collect a large number of oscillations to get a thickness calibration as accurate as possible. Finally, the single layer thicknesses, previously determined by the fitting of the XRR measurements, were divided by the respective deposition time to obtain the refined deposition rates of the targets (about 0.07 nm/s). The application of pre-sputtering process and the confirmation of the deposition rate stable condition (displayed by the quartz microbalance) always precede the deposition of the sample layers. It turns out that, with the exception of the Ta cover layer exposed to oxidation, the actual thickness values of the samples are very close to the nominal values, which validates the protocol. In order to have an in-plane crystallographic reference, a mark on the non-polished backside of the substrate was done aligned to the primary flat ⟨110⟩ direction of the Si(100) wafer. The samples were kept in vacuum immediately after the preparation and during the intervals between the measurements.

X-ray diffraction (XRD), in a Bragg-Bretano Geometry (divergence slit = 3 mm, scattering slit = 3 mm and receiving slit = 0.3 mm), and grazing incidence X-ray diffraction (GIXRD), in a Parallel Beam Geometry with a parallel slit analyzer (divergence slit = 0.1 mm, scattering slit = receiving slit = 7 mm), patterns were recorded using an Ultima IV Rigaku diffractometer. X-ray reflectivity (XRR) patterns were recorded using a Discovery D8 Bruker diffractometer (θ/2θ goniometer, divergence slit = 0.06 mm, receiving slit = 7 mm). Both the diffractometers operated at RT with the Cu-K_α radiation (λ = 1.5418 Å). The XRR patterns were fitted using the Dyna code in the Parrat's formalism mode [51]. Magnetization measurements as a function of the applied field M(H) were recorded using Quantum Design SQUID MPMS XL (for most the measures) or Quantum Design SQUID-VSM (for measures at the thermal analysis subsection) magnetometers. Three different type of thermal protocols have been applied during the magnetization experiments: 1) zero field heating (ZFH) – heating the sample without an applied magnetic field, 2) field cooling (FC) – cooling the sample down to RT under a $\mu_0 H$ of 0.05 T applied along the in-plane direction making a desired φ angle with the reference mark and 3) zero field cooling (ZFC) - cooling the sample without an applied magnetic field (remnant mode). It is important to emphasize that before a ZFH or ZFC protocol, an oscillating field process was applied to remove remnant fields from the superconductor coil. No substantial changes were observed in the RT M (H) loops for virgin and FC (from 400 K to 300 K) Samples A and B with the field aligned to the primary flat ⟨110⟩ direction of the substrate (this orientation was chosen for the test) taken after more than one year. This experimental observation informs that no substantial training or aging effects are present in our samples.

III. Results and discussion

A. Magnetization

RT normalized M(H) loops of the as-prepared Sample A (prior any application of a thermal protocol) were obtained for different orientations depending on the angle φ (0°, 30°, 45°, 60°, 90°, 120°, 135°, 150° and 180°) between the direction of the in-plane applied magnetic field and the reference mark of the substrate. Two representative loops (φ = 0° and 90°) are plotted in Fig. 1. The maximum amplitude for the magnetic field $\mu_0 H$ was 0.5 T. The M(H) loops are composed of two distinct regions presenting different characteristics. The central part of the M(H) loop shows an abrupt magnetic reversal for very small magnetic fields, with a maximum ratio of susceptibility (namely χ_{max}) and low $\mu_0 H_C$ coercivity, as expected for the Py (≈ 8 x 10^{-4} T). This reversal is more pronounced for φ = 0° rather than φ = 90° [*see the insert of* Fig. 1]. The other regions on each side is characterized by a slow increase of the magnetization at high fields 0.2–0.3 T. The saturation field $\mu_0 H_{sat}$ (defined here as the magnetic field leading to 95% of the saturation magnetization) increased from 217.8 mT to 262.5 mT when the φ–parameter goes from φ = 0° to φ = 90°. In addition, the magnetization at remanence (M_R) is lowered from 49.4% to 33.2% when φ parameter varies from 0° to 90°. The observation of the two regions in the M(H) loops of Sample A are linked to the presence of two magnetic phases with different chemical compositions along the growth axis, as will be proved later by the XRR results. From the magnetic characteristics, and in particular from the maximum of susceptibility:

$$\chi_{max} = \left\{ \mathbf{d}\left(\mathbf{M}/\mathbf{M_S}\right)/\mathbf{d}\mu_0\mathbf{H} \right\}_{max} \quad (4)$$

the axis defined by φ = 0° is an easier axis of magnetization than that corresponding to φ = 90°.

Fig. 2 shows the φ angle dependence of the magnetic parameters for Sample A: M_R, χ_{max} and $\mu_0 H_{sat}$, derived from the M(H) loops. Here, these values are estimated from the average of descending and ascending branches. An oscillation of these magnetic parameters is observed, and the hard and easy axes are out-of-phase by 90°, indicating that the magnetic system has a K_U anisotropy. As expected, $\mu_0 H_{sat}$ and (M_R, χ_{max}) are in antiphase with φ. Based on Eq. (2), a simple uniaxial law: $a + b.\sin^2(\varphi + c)$ with 3 constants (a,b,c) is used for fitting the $M_R(\varphi)$, $\mu_0 H_{sat}(\varphi)$ and $\chi_{max}(\varphi)$ curves [27]. The full lines in Fig.2 are the best obtained fits, where the fitted laws are indicated in Fig. 2. From the fits, the difference of phases between $\mu_0 H_{sat}$ and M_R (or χ_{max}) is close to 90°, as expected. The average values extracted from the fits for the easy and hard axes of the magnetization are, respectively, φ = 3 ± 7° and 93 ± 7° Thus,

UNCORRECTED PROOF

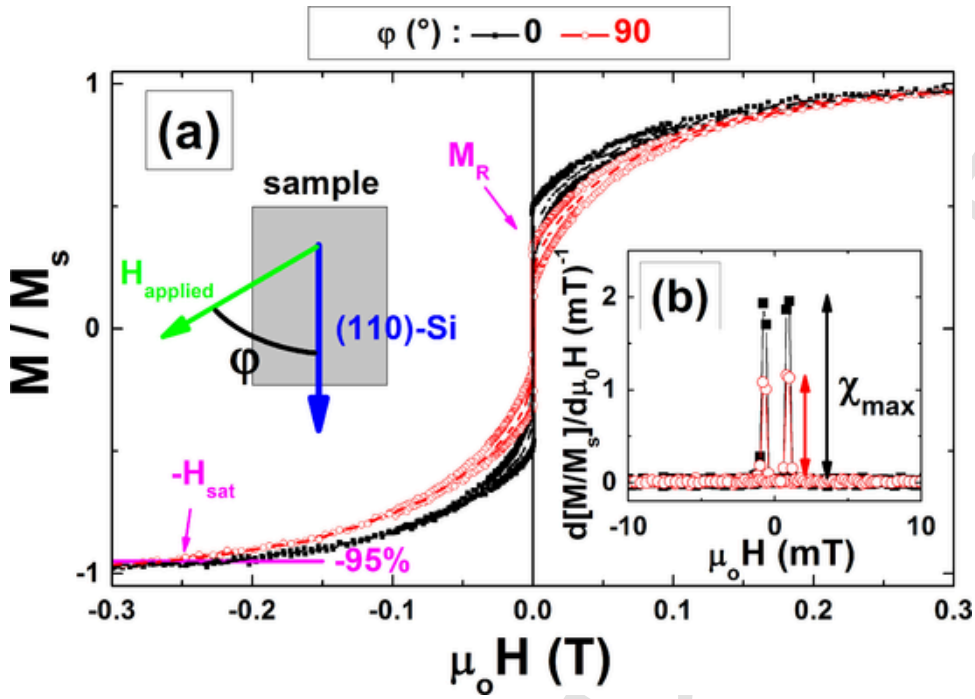

FIG. 1. (a) RT normalized M(H) magnetic loops of the as-prepared Sample A for two different geometries of measurements (φ = 0° and φ = 90°). The magnetization at remanence M_R and the saturation field H_{sat} taken at $M/M_S = -95\%$ indicate an easy axis more pronounced for φ = 0° The dashed lines are the mean magnetization between decreasing and increasing branches leading to the calculation of the anisotropy constant (see text). (b) Zoom of the derivative of M/M_S as a function of H [with a maximum susceptibility χ_{max} stronger for φ = 0° also indicating this easy axis].

the M(H) loops presented in Fig. 1 can be considered, within the experimental error, as obtained along the easy (black loop) or hard (red loop) axes of the magnetization.

The in-plane effective anisotropy constant of the FM layer K_1^{FM} being defined as:

$$\int_0^{H_{max}} \mu_0 \left[M(H, \varphi = 0^\circ) - M(H, \varphi = 90^\circ)\right] dH \tag{5}$$

is estimated from the M(H) loops in Fig.1. $\mu_0 H_{max} = 0.5$ T was considered sufficient for the integration since $\mu_0 H_{sat}$ ranges from 217.75 mT to 262.54 mT. By averaging the descending and ascending branches of the magnetic hysteresis for the two geometries of measurements (dashed lines in Fig. 1) and by using the previous formula, the value of the effective anisotropy constant $K_1^{FM} = (1.1 \pm 0.5) \times 10^4$ J/m^3 is calculated. Since the in-plane effective anisotropy energy K_{eff}^{FM} has the uniaxial form and the magnetization is in the sample plane, the following relation is valid:

$$K_{eff}^{FM} \approx -\frac{\mu_0}{2} M_S^2 + K_U = -\frac{\mu_0}{2} M_S^2 + K_1^{FM} sin^2\omega, \tag{6}$$

where ω is defined in the introduction part. The contribution of the fcc K_{MA} anisotropy (≈ - 2.7 × 10^2 J/m^3 for Py) [28, 32, 33] and other minority terms to K_1^{FM} are too low and are not considered in Eq. (6).

Therefore:

$$K_{eff}^{FM} = \left[-(3.5 \pm 0.6) \times 10^5 + (1.1 \pm 0.5) \times 10^4 sin^2\omega\right] J/m^3 \tag{7}$$

This result indicates that the FM moments are in the film plane and along $\boldsymbol{K_U}$ for $H = 0$. In addition, K_U is attributed to the elongated FM grains formed by the shadowing effect due to the oblique incidence of the sputtering flux, even though the growth was performed in the 0.5 Hz spin deposition mode, as already detected for thicker Co layers [24, 26].

Fig. 3 displays the RT normalized M(H) loops of the as-prepared Sample B (black open symbols) and of Sample B after a FC process (red filled circles), performed following a ZFH treatment from 300 K to 400 K. These set of M(H) loops were measured for different orientations of the applied field φ = 0° [Fig. 3(a)], φ = 30° [Fig. 3(b)], φ = 45° [Fig. 3(c)], and φ = 70° [Fig. 3(d)]. The −20°-M(H) [Fig. 3(e)] and 90°-M(H) [Fig. 3(f)] loops are also added in inset of Fig. 3(a) and Fig. 3(d), respectively. It is important to point out that different parts of the as-prepared Sample B were used to record the M(H) loops for each φ in order to prevent undesirable magnetic memory effects. Otherwise, the spin configuration stabilized after the ZFH/FC protocols for φ = 0°, for example, would severely affect the measurements under other subsequent magnetic field orientations. Thus, the M(H) loops were obtained after each piece of sample B has been subjected to the same protocol. A maximum $\mu_0 H$ field was 0.3 T was used. The shape and the φ-dependent variations of the M(H) loops exhibit more features for Sample B than for Sample A, which result from the interplay between the IrMn AF film and the Py film.

Regarding the as-prepared samples, the M(H) loops are not centered along the field axis (the inset of Fig. 3 provides a zoom of the area around zero field). This scenario is quite unusual for ultrathin unbiased FM films with in-plane magnetization. No M(H) loops shifts (no exchange bias) should be observed in absence of field cooling process or deposition in zero applied magnetic field. This indicates the presence of an unexpected anisotropy ($K_{eff}^{FM/AF}$). It should be remembered that, due to the rotation of the sample during the deposition, the action of any undesirable magnetic field from the magnetrons could effectively be disregarded. In addition, the amplitude of the M(H) loop shift depends on φ. These hysteresis loops for the as-prepared Sample B were obtained starting from positive to negative fields. In this case, the initial shift to the right or left along the field axis depends on the sample orientation regarding the field direction of the magnetometer. Even when the sample is oriented out of the easy axis, we can assume its positive or negative component (except for perpendicular alignment when negligible shifts are expected). In addition, positive or negative signal for com-

UNCORRECTED

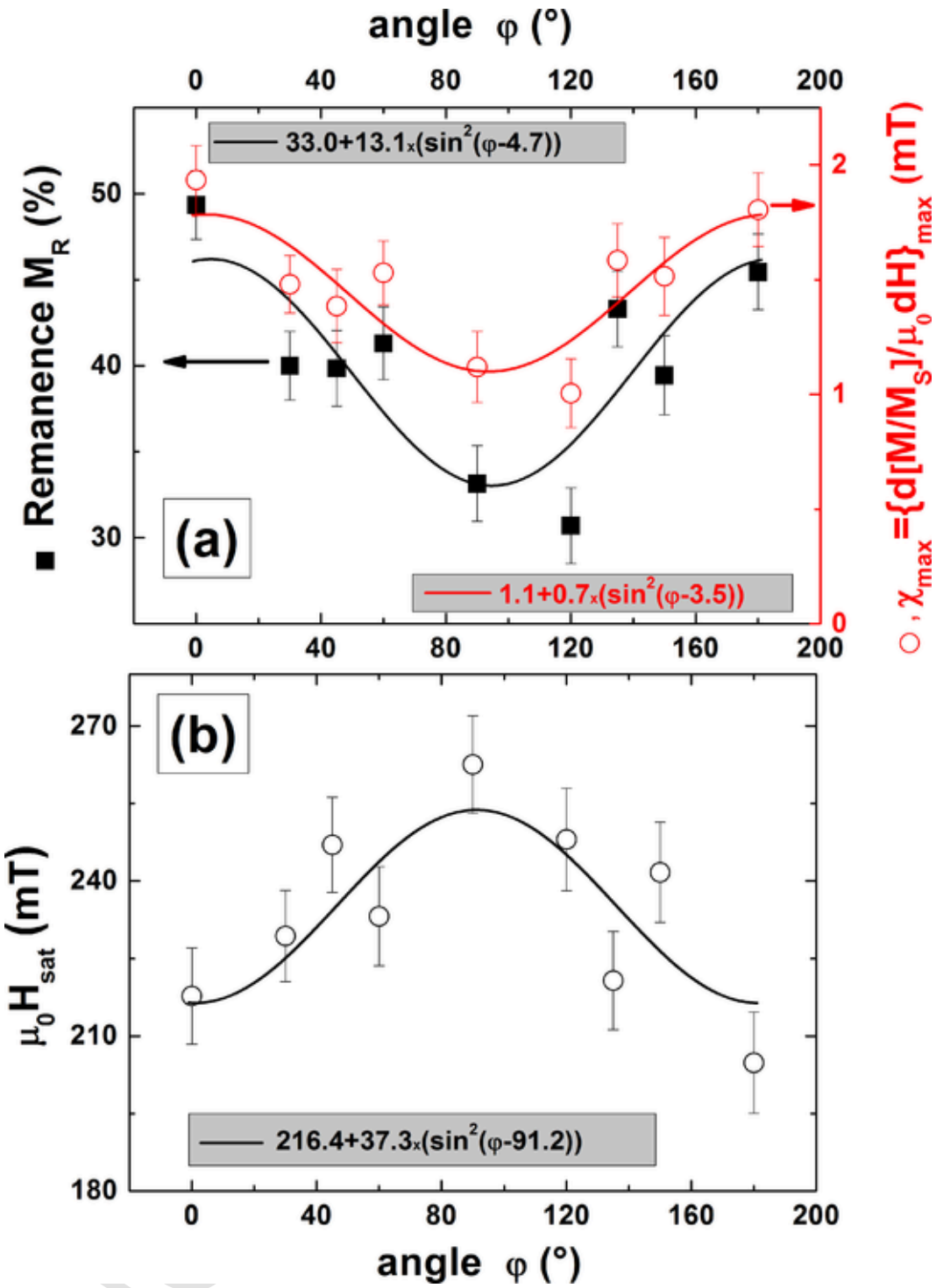

FIG.. 2. Evolution following the angle φ for the as-prepared Si(100)/Ta(3 nm)/Py(3 nm)/Ta(3 nm) multilayer (Sample A) at RT for the (a) remanence M_R (left-part) and maximum susceptibility χ_{max} (right-part); (b) saturation magnetic field $\mu_0 H_{sat}$. The straight lines are corresponding to best adjustments by taking account a simple uniaxial anisotropy as the form $a + b.\sin^2(\varphi + c)$) with a, b and c constants (fitted laws are indicated in the graphs).

ponent of the as-prepared effective anisotropy can be previewed by checking the remnant magnetization of the virgin sample (before to initiate the measurement at zero field achieved by oscillating the field from high fields). Thus, if two virgin pieces of the same sample is inserted with the same orientation regarding the field direction of the magnetometer, and if we start from negative or positive fields, the resultant loops are very similar with no systematic change. In addition, it should be kept in mind that ZFH/FC measurements are always performed after measuring the as-prepared sample and under positive fields. After the ZFH/FC protocol, the magnetic loops were shifted to the left relatively to the loops obtained for the as-prepared samples. That is generally expected for positive magnetic fields applied during the FC protocol. The amplitude and uniformity of the loops were also dependent on φ.

The coercive $\mu_0 H_C = \left|\left(\mu_0 H_{C,1} - \mu_0 H_{C,2}\right)\right| /2$and the displacing $\mu_0 H_d = \left(\mu_0 H_{C,1} + \mu_0 H_{C,2}\right) /2$ fields, extracted from the RT M(H) loops in Fig.3, are presented in Table I. Here, $\mu_0 H_{C,1}$and $\mu_0 H_{C,2}$ designate, re-

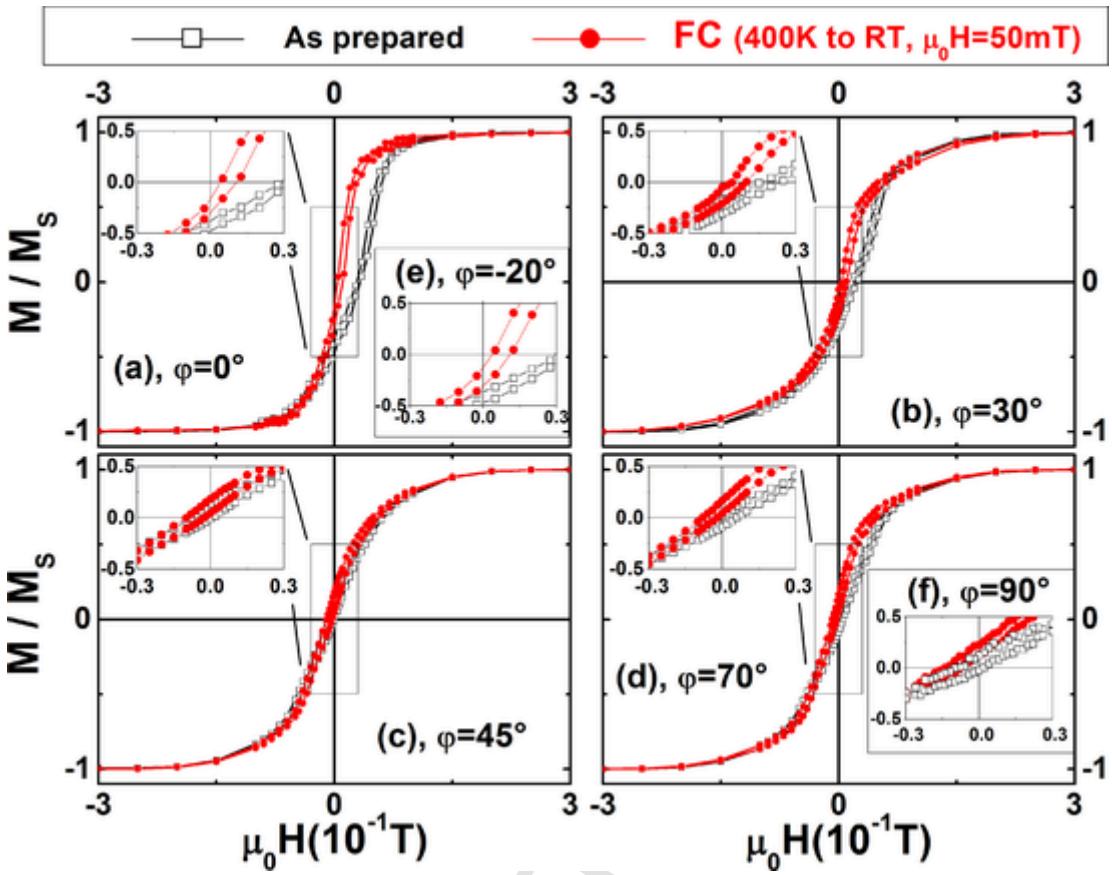

FIG.. 3. (a-b-c-d-e-f) As-prepared (black open symbols) and field cooled (red filled circles, $T_{max} = 400$ K and $\mu_0H = 50$ mT) RT normalized M(H) loops of the Si (100)/Ta(3 nm)/Py(3 nm)/IrMn(8 nm)/Ta(1 nm) multilayer (sample B) for different values of φ comprised between 0 and 90° The inset shows a zoom of central parts of the hysteresis loops (see the exchange bias effects).

TABLE I
Coercive field μ_0H_C and displacing field μ_0H_d fields extracted from the M(H) loops of Fig.3 (as-prepared and after FC procedure) as a function of φ. $\Delta\mu_0H_d$ is defined by μ_0H_d(FC)- μ_0H_d (as-prepared). The uncertainties in the field values are ±0.3 mT (±0.6 mT for $\Delta\mu_0H_d$).

Sample B					
Procedures	as-prepared	FC	as-prepared	FC	
Field direction φ (°)	μ_0H_C (mT)	μ_0H_C (mT)	μ_0H_d (mT)	μ_0H_d (mT)	$\Delta\mu_0H_d$ (mT)
−20	3.2	3.6	32.5	7.4	−25.1
0	2.2	3.2	30.6	7.0	−23.6
30	3.9	3.0	20.4	7.1	−13.3
45	4.3	3.6	−3.7	−6.3	−2.6
70	3.9	3.0	1.7	−5.5	−7.2
90	5.5	3.2	−3.7	−10.8	−7.1

spectively, the coercive fields for the ascending and descending branches of the M(H) loops. The lowest (highest) coercivity for the as-prepared procedure is recorded for φ = 0° (φ = 90°), whereas it remains relatively constant for the FC procedure, within their uncertainties, whatever the φ value. Concerning the displacing field, its modulus is larger (smaller) for φ = −20° (φ = 70°) for the as-prepared sample. In the last case, we have chosen to discuss only the amplitude of the shifts since the negative sign for φ = 45° and φ = 90° originates from the orientation of the sample when inserted in the SQUID magnetometer as explained in the last paragraph.

In order to show quantitatively the effect of the application of the ZFH/FC protocol on the displacing field, we introduce the $\Delta\mu_0H_d$ parameter [defined as μ_0H_d(FC)-μ_0H_d(as-prepared)]. Its value is always negative, reflecting the negative EB effect where the M(H) loops shift to the left-hand side along the field axis as expected. In addition, the largest value of $|\Delta\mu_0H_d|$ is reached for φ = −20° and it tends to decrease as φ increases. Therefore, it is possible to infer that the ZFH/FC protocol is able to change partially the $K_{eff}^{FM/AF}$ anisotropy, since it induces a modification on the configuration of the pinned FM interfacial moments.

The analysis of the χ_{max} and μ_0H_{sat} quantities was also done similarly to that performed for Sample A. Thus, the χ_{max} [in $(mT)^{-1}$] values are simultaneously (0.031–0.031–0.023–0.018–0.016–0.017) and (0.040–0.043–0.037–0.020–0.022–0.020), while the μ_0H_{sat} (in mT) parameter reaches (35.8–130.0–174.0–180.4–187.0–159.6) and (90.0–140.0–200.2–178.6–185.8–161.2) when the φ angle is varied in the from −20 to 90° for the as-prepared and FC samples, respectively.

As for the Sample A, χ_{max} is progressively decreased, whereas the μ_0H_{sat} parameter is progressively enhanced. By fitting the experimental data of the quantities χ_{max} and μ_0H_{sat} with the same law used to fit the results from Sample A, it was found for the as-prepared sample B that the easy axis of the total anisotropy $K_{eff}^{FM/AF}$ forms an angle φ = - 24 ± 9° with **H** and that the hard axis forms an angle φ = 66 ± 9°, about 90° apart as for the Py layer alone. This is consistent with the φ dependence of the μ_0H_C, $|\mu_0H_d|$ and $|\Delta\mu_0H_d|$ parameters. As a consequence, the particular uniaxial magnetic anisotropic characteristic persists when an IrMn layer is added in the stack. The uniaxial anisotropy is also detected after the ZFH/FC protocols. In this case, the $K_{eff}^{FM/IAF}$ easy axis is around φ = (- 10 ± 10°), proving that the ZFH/FC protocol can change the orientation of the pinned FM spins. Since Sample A and Sample B

UNCORRECTED

are different specimens, there are two possible explanations for the difference between the angular positions of their easy anisotropy axes: (i) the mean orientations of the elongated grains respect to the reference mark in the substrates are different, an extrinsic effect arising from the deposition process and/or (ii) there is a redirection of the FM moments due to a magnetic coupling emerging at the FM/AF interface (intrinsic effect).

Now, it is possible to discuss the origin of the H_d field and $K_{eff}^{FM/AF}$ in the as-prepared Sample B. Actually, the spontaneous magnetization of the FM Py film, pointing in its K_{eff}^{FM} (K_U) easy axis direction, pins the IrMn moments to the Py ones, as soon as the AF order is established. Consequently, a K_{EB} is set at the interface. Based on this assumption, the shift and shape of the M(H) loops of the Sample B depends on the relative orientation between the **H** field direction and the $K_{eff}^{FM/AF}$ easy axis.

B. Structural investigation

In order to provide a better insight into the interpretation of the magnetic results of Samples A and B, we examined their structure in detail by XRD, GIXRD or XRR and compared these results to a control sample.

The GIXRD pattern of Sample A [Fig. 4(a)] taken for an incident angle of $\alpha = 0.5°$ (very close to the critical angle) revealed reflections relative to the β-Ta body centered tetragonal (bct) structure and (111) preferentially oriented fcc Py planes. The β-Ta phase was initially stabilized as islands on the Si wafer due to interface energy minimization before the columnar growth with a strong [001] fiber-texture [52]. No reflection was found related to Ta or Py layer after $2\theta = 50°$ in this GIXRD pattern. For $\alpha = 2°$ and 3°, the background from the substrate suppressed the weak and broad lines related to the ultrathin first Ta layer and Py layer. In addition, Ta and Py reflections are absent in the conventional (θ−2θ) XRD pattern. The diffraction lines become broader and weaker, as the layer thickness decreases, making the structural analysis more difficult in ultrathin films. However, we tried to discuss our results by making comparison with those obtained for thicker reference samples. The XRD pattern of a Si(100)/Ta(20 nm) sample [Fig. 4 (b)] reveals that the β-Ta structure grows with a [001] preferential orientation on the silicon substrate in order to match the lattice parameters ($a = 5.543$ Å for Si and $a = b = 10.194$ Å and $c = 5.313$ Å for Ta). Thicker Py layers tend to grow on Si(100)/Ta with a [111] preferential orientation, as will be discussed later. Since the Py (111) reflection is also seen in the GIXRD ($\alpha = 0.5°$) pattern (very low intensity) of Sample A, we can infer that although a thicker Py layer has a tendency to grow with a [111] preferential orientation, the analysis on the ultrathin Py layer in Sample A cannot rule out that the Py {111} planes also aligned in other directions.

The XRR pattern of Sample A [Fig. 4(c)] has been fit with two different models: Fit-A (green line), which considers a Si/Ta/Py/Ta/$Ta_{29}O_{71}$ stack which includes the partial oxidation of the Ta capping layer, and Fit-B (red line), which, in addition assumes a NiFeTa layer formed by the atomic diffusion at the bottom Ta/Py interface. The tantalum pentoxide ($Ta_{29}O_{71}$) is the most stable Ta oxide [53, 54] and it was included on the top of the stack to account for the oxidized part of the capping layer, since the XRR experiments were performed ex-situ. Indeed, the consideration of its existence improved the fittings (A and B). In addition, we have to emphasize that the Ta surface passivation, by ultrathin native Ta oxides, has been detected in nanoparticles, thin films, wires and bulk materials [55 - 58]. More specifically, results from the literature [56, 57] have shown that the X-ray photoelectron spectroscopy provided a sublayer resolution for the natural oxidation of the polycrystalline Ta surface [Ta/TaO clusters in Ta matrix (2 nm)/$Ta_{29}O_{71}$ (3 nm)] [56], while two sublayers of different oxides has been found in ultrathin Si/SiO_2/Pt/Co/Ta/MgO/TaO_x by X-ray reflectivity techniques [57]. They have also shown that the oxidation process increased the original metallic Ta lattice parameter, resulting in a thicker oxide layer (from 2 nm thick Ta to 3.8 nm thick $Ta_{29}O_{71}$) [57]. This observation fully agrees with our results obtained from the XRR data fitting. Although the simpler model (Fit-A – green line) fits relatively well the experimental data, some features are not reproduced as the high angle side of the oscillation at 2q = 5° In addition, the best

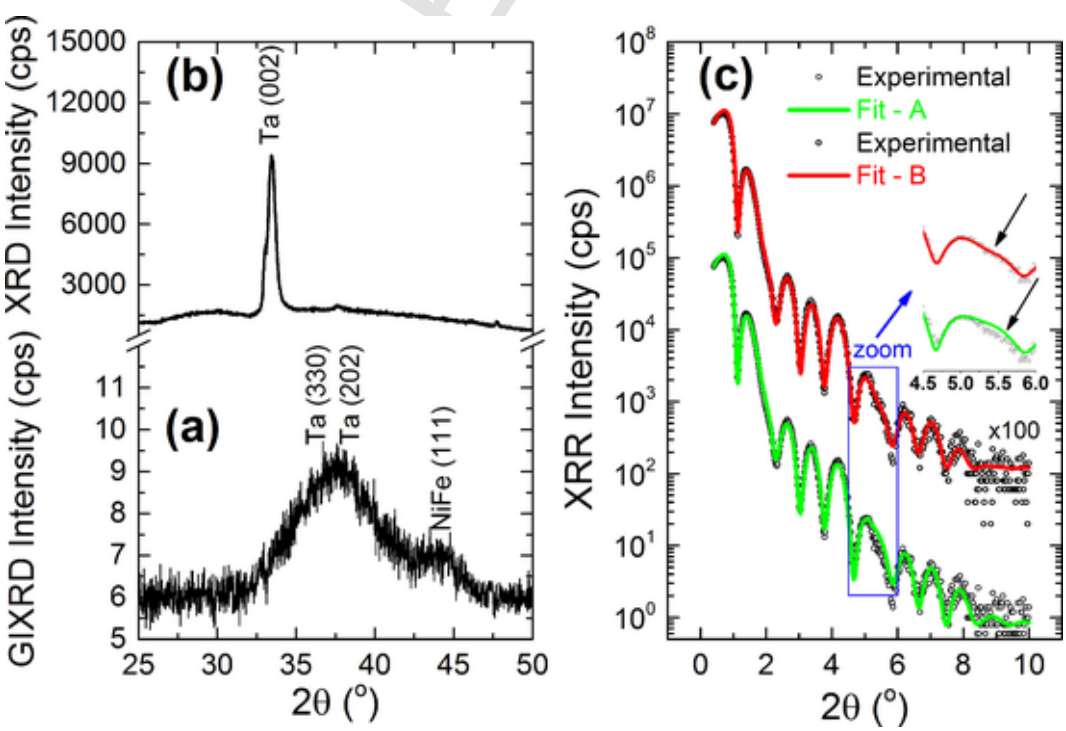

FIG.. 4. (a) RT GIXRD pattern for the Sample A for an incident angle $\alpha = 0.5°$ (b) XRR pattern of the Sample A (black open circle) and the respective Fit - A (green line) and Fit – B (red line).

function value (χ_{Best}) for the Nelder-Mead Simplex algorithm [59] used as an optimization method for the FIT-A was $\chi_{Best} \approx 8.5$. When the interlayer phase at the bottom Ta/Py interface was inserted (Fit-B), the fit became much better and the χ_{Best} value decreased to 3.2.

Tables II show the structural parameters derived from the XRR pattern of Sample A [Fig. 4(c)] using Fit-B. The real (f') and imaginary (f") energy dependent corrective terms to the scattering factors have been obtained from literature [60, 61]. The t_n parameter denotes the nominal thickness, t is the thickness value obtained from the fit, σ is the root-mean-square roughness and ρ is the material density. The densities were compatible with the nominal values within the error bar, considering that the densities in ultrathin films can vary about 10–15% from the bulk standard values. The interface roughness varied from 0.2 to 0.5 nm (values characteristics of flat interfaces). The thicknesses are in agreement with the nominal values within error, except for the capping layer. However, it is necessary also to consider that the capping layer thickness tends to increase its value when the oxygen reacts with Ta to form the $Ta_{29}O_{71}$ oxide. A NiFeTa sub-layer, due to an atomic diffusion at the bottom Ta/Py interface, should be inserted in the structural model in order to significantly improve the fit. It should be pointed out that considering the insertion of an alloy layer at the upper Py/Ta interface did not improve the fit and the adjustment procedure tends always to decrease the NiFeTa thickness towards zero. Therefore, the existence of a NiFeTa alloy layer only develops at the lower interface and the possibility of interdiffusion at the upper interface is limited and properly accounted for by the roughness.

TABLE II
Model B fit parameters (thickness t, with t_n as the nominal one, roughness σ and density ρ) extracted from the XRR pattern of the as-prepared Sample A. Uncertainties are in the parenthesis, and the expected density is given in square brackets.

Sample A				
layers	t_n (nm)	t (nm)	σ (nm)	ρ (g/cm^3)
$Ta_{29}O_{71}$		2.4 (0.9)	1.0(0.2)	7.2(0.7) [8.37]
Ta	3.0	2.8(0.2)	0.3(0.2)	14.4(1.5) [16.05]
$Ni_{80}Fe_{20}$	3.0	2.7(0.4)	0.4(0.1)	8.2(0.8) [8.69]
$Ni_{40}Fe_{10}Ta_{50}$		0.8(0.4)	0.6(0.2)	13.2(1.0) [13.17]
Ta(buffer)	3.0	3.2(0.5)	0.3(0.2)	15.7(1.5) [16.05]
Si(100)			0.3(0.1)	2.33(0.02) [2.33]

The RT XRD pattern of the Sample B [Fig. 5(a)] shows the reflection line of the [111] preferentially oriented fcc IrMn film. The (111) reflection peak of the IrMn (green line) is positioned at 2θ = 41.18(0.02)° and shows a diffuse intensity, mainly on the wide angle side, which can be attributed to Pendellösung fringes, obeying the following relation:

$$I(q) = \left[\sin\left(qnd_{111}/2\right) / \sin\left(qd_{111}/2\right)\right]^2, \quad (8)$$

where $q = 4\pi sin\theta/\lambda$, d_{111} is the (111) interplane distance of the IrMn phase and n is the number of planes, *nd* being the product equal to the IrMn thickness (t_{IrMn}). The presence of Pendellösung fringes in the first order reflection indicates that the atomic planes within the IrMn layer are well stacked along the (111) direction, normal to the film plane, and exhibits relatively flat interfaces. This fact is corroborated by the presence of the second order reflection (222) peak at 2θ = 89.38(0.04)° (not shown). The fit of the Pendellösung fringes leads to the following structural parameters: d = 0.2193(0.0001) nm, n = 35 and $t_{Ir20Mn80}$ = 7.7(0.2) nm; a thickness value that agrees with the nominal one (8 nm). Moreover, the fringes appearing in Sample B also emerges very clear in a Si(100)/Ta(3 nm)/Py(3 nm)/IrMn(7 nm)/Co(2 nm)/Ta (1 nm) multilayer, which is outside the scope of this study, but will be published elsewhere. The peaks from the Ta and Py layers have not been observed in the pattern illustrated in Fig. 4(a).

In order to understand how Ta and Py grew in the stacking, the RT XRD pattern of a thicker Si(100)/Ta(10 nm)/Py(20 nm)/IrMn(15 nm)/Ta(5 nm) has also been measured and is shown in Fig. 5(b). This indicates that the Py and IrMn layers tend to grow with a [111] preferential orientation on the (002) planes of the tetragonal Ta buffer layer. Since we know that the β-Ta buffer tends to grow on Si(100) with a [001] ori-

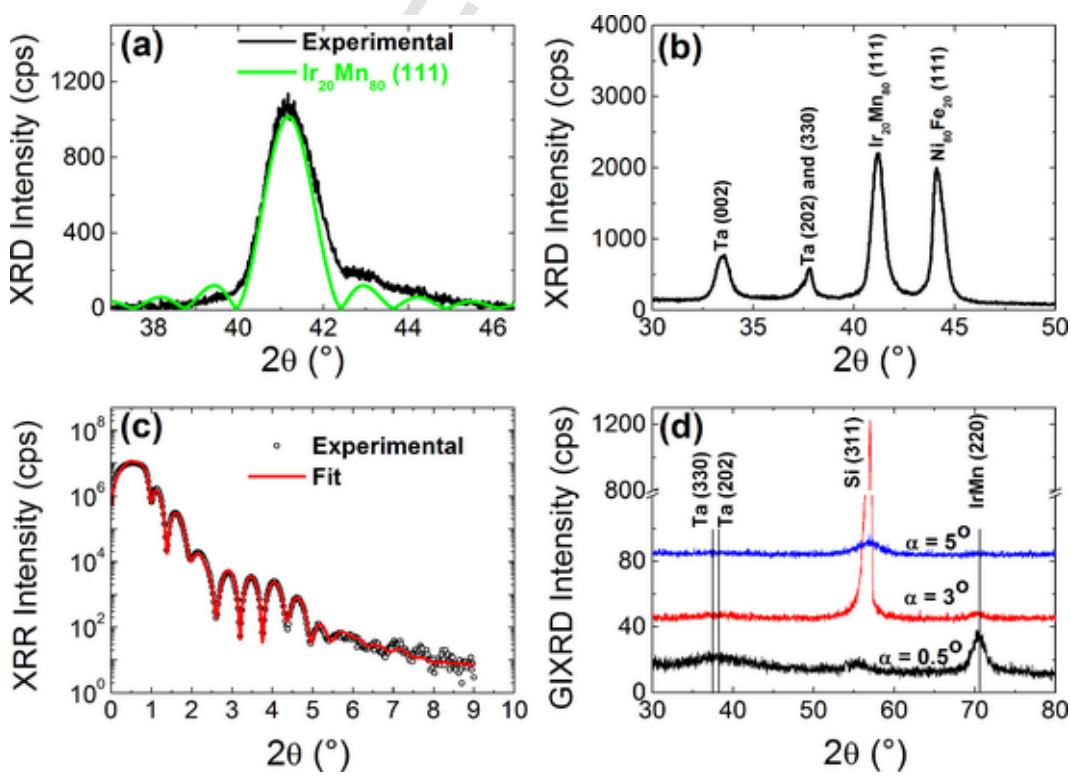

FIG.. 5. (a) RT XRD pattern for the Sample B. (b) RT XRD pattern for a thicker Si(100)/Ta(10 nm)/Py(20 nm)/IrMn(15 nm)/Ta(5 nm). (c) XRR pattern of the Sample B (black open circle) and the respective Fit (red line). (d) RT GIXRD pattern for the Sample B for incident angles α = 0.5°, 3° (red), 5° (blue).

entation [(002) reflection line in the XRD pattern], as already discussed for Sample A, the (202) and (333) reflections lines can be associated with the Ta capping layer. Certainly, the analysis from thicker samples did not show the details existent in the first stacked monolayers, as can be detected in case of ultrathin films, however, it illustrates the growth tendency.

The GIXRD pattern of Sample B, taken at $\alpha = 0.5°$ [(Fig. 5(d)], also presents the Ta (330) and (202) reflections, but there is no reflection from the NiFe layer. As the angle of incidence α is very close to the critical angle, we assume that these Ta reflections originate mainly from the capping layer. In addition, the (220) reflection line from the IrMn layer [$2\theta = 70.51(0.02)°$] appeared in the GIXRD patterns from $\alpha = 0.5°$ to $\alpha = 3°$ This is expected for the well stacked (111) preferentially oriented fcc-IrMn layer since the angles between the (220) and (111) planes (face centered cubic structure) is about 35.3°, the θ Bragg angle for the IrMn (220) reflection is about 35.25° and the (111) planes are preferentially parallel to the sample surface.

The GIXRD results of Samples A and B clearly show that the [111] orientation distribution for the Py layer (around the normal to the sample surface) is wider than that for the IrMn one. This conclusion is based on the following points: 1) Py and IrMn layers tend to grown with a [111] preferential orientation as observed in the thick sample and in Sample B for IrMn (seen by θ−2θ XRD diffraction) and 2) the (111) Py (IrMn) line is present (absent) in the Sample A (Sample B) GIXRD pattern. In other words, the results indicate that the Py layer shows a wide dispersion of the crystalline orientation for the first stacked monolayers (ultrathin limit), probably due to interface effects, such as: lattice parameters mismatch, atomic diffusion, and also the ultrathin thickness of the Ta seed layer (3 nm). The detection of these details was possible because the Ta and Py films are in the ultrathin regime. Certainly, the Py (111) texture will become higher for thicker Ta and Py layers, but the presented detail would be hidden. Some of us have demonstrated that the (111) Py texture is strongly enhanced for Ta buffer layers and for Py layers thicker or equal than 10 nm and 20 nm, respectively [20]. The role of the interface effects will become clearer during the XRR discussion. In addition, it is important to point out that the structural order of the ultrathin Py layer in Sample B is good enough to allow the growth of an IrMn layer with relatively very well stacked (111) planes, indicating that the Py layer is better organized at the upper interface than at the lower interface with the Ta layer, which is consistent with a NiFeTa layer essentially present at the lower interface in sample A.

The RT reflectivity curve (XRR) for Sample B and the respective fit derived from the same model B used to fit Sample A are displayed in Fig. 5(c). The parameters extracted for the best Fit-B model, are presented in Table III.

The thicknesses of the layers correspond to the expected values within the error bar. The 7% reduction of the mean thickness of the Py layer is due to the need to take into account an intermixed $Ni_{40}Fe_{10}Ta_{50}$ layer. Nevertheless, the total thickness of Py, $Ni_{40}Fe_{10}Ta_{50}$ and Ta (buffer) layers differ only by 3% whether we sum the Py and Ta(buffer) nominal thicknesses. The roughness values are limited between 0.3 and 0.5 nm which indicates good layer stacking quality. The material densities are in agreement with the bulk values within the error bars.

TABLE III

Model B fit parameters (thickness t with t_n as the nominal one, roughness σ and density ρ) extracted from the XRR pattern of the as-prepared Sample B. Uncertainties are in the parenthesis, and the expected density is given in square brackets. The asterisk indicates the nominal thickness is related to the deposited Ta layer, but the corresponding parameters obtained from the fit are associated with the completely oxidized $Ta_{29}O_{71}$ layer.

As-prepared Sample B				
layers	t_n (nm)	t (nm)	σ (nm)	ρ (g/cm^3)
Ta* - $Ta_{29}O_{71}$	1.0*	2.4 (0.2)	0.5(0.1)	8.9(1.3) [8.37]
$Ir_{20}Mn_{80}$	8.0	7.8(0.4)	0.4(0.2)	10.3(0.1) [10.28]
Py	3.0	2.8(0.4)	0.4(0.1)	8.0(0.8) [8.69]
$Ni_{40}Fe_{10}Ta_{50}$		0.9(0.4)	0.5(0.1)	13.7(1.0) [13.17]
Ta(buffer)	3.0	2.5(0.5)	0.5(0.2)	14.4(1.6) [16.05]
Si(100)			0.3(0.1)	2.33(0.02) [2.33]

Based on the structural analysis, it can be deduced that the atomic diffusion between Py and Ta, which occurred during deposition, formed an intermediate layer of NiFeTa alloy at the lower Ta/Py interface. Although it is very likely that the NiFeTa alloy has not a constant composition along the growth axis within the 0.9 nm, we supposed it does not have a substantial change along 2 or 3 monolayers. For the fit, we used an average composition with $Ni_{40}Fe_{10}Ta_{50}$. Therefore, the Py layer can be considered as composed of bottom (NiFeTa alloy) and top (Py sublayer) regions, being responsible for the peculiar M(H) loop shape of the Samples A and B, where there are abrupt magnetization reversions at the central part of the loops (top Py sublayer) and other region harder to saturate with an unusual saturation field intensity as a response to the bottom Ta/Py interface (Fig. 1 and Fig. 3). The detection of this alloyed NiFeTa layer at the Ta/Py interface was only possible because the film is in the ultrathin limit. It is reported in the literature [62] that a co-sputtered thin NiFeTa layer has a K_U constant much higher than the one for the uniform Py layer. Both the samples were deposited under an external magnetic field. The authors show that the small anisotropy of the uniform Py layer was only induced by the magnetic field applied during the deposition while the increase of anisotropy for the laterally composition-graded NiFeTa layer was attributed to a stress-induced effect, although the compositional gradient is very small along the hard axis, where the Ni, Fe and Ta contents varied only from 72.5% to 71.1%, from 15.5% to 14.9% and from 12.0% to 14.0% (within the error bar of ± 0.5%) over 1 cm, respectively. Nevertheless, they did not discuss the influence of the oblique deposition of the sputtering flux coming from the lateral region of the solid angle sputtered by the Ta target during the co-deposition, where the shadow effect can play an important role. In our case, the K_U anisotropy was set along the elongated grains of the laterally uniform (Py + NiFeTa) layer formed by the shadow effect, and besides that, we can affirm the K_{eff} constant of the (bottom NiFeTa alloy + top Py sublayer) ferromagnetic system is higher than that for a pure Py layer. In other words, we can say that the presence of the NiFeTa alloy hardens the ferromagnetic anisotropy. It can also be recalled that the offset of the hysteresis loops (anomalous shift) in Fig. 3 set without any field applied during the multilayer growth or any FC protocol applied posteriorly after the sample preparation may have its origin in this hardening of the FM layer, as it was observed in literature [63] where an exchange bias was set by only the stress-induced effect in a NiFeTa/IrMn system with a laterally composition-graded 150 nm ticker NiFeTa layer. From the magnetic behavior of the top Py sublayer observed in Fig. 1 (for Sample A), it can be predicted that the uniform layer of pure Py (in Sample B) would not have a sufficiently strong K_{eff} constant to set an $E_B$in this system when the substrate holder is rotated at 0.5 Hz and no magnetic field is applied during the deposition.

C. Thermal analysis

Magnetic measurements were carried out at high temperature to investigate the effect of heat treatment on the anomalous shift effect, in particular to try to minimize it. The effect of temperature on the structure of the system and in particular on changes at the interfaces was also studied. The ZFH and ZFC protocols were applied to a virgin piece of the Sample B between RT and 600 K. The higher limit temperature of 600 K was chosen because it is above T_B of the γ-IrMn phase (520 K to 590 K depending on the preparation method) [43]. The sample was rotated around its normal axis so that the [110] direction of the substrate forms an angle of 70° with the direction of the H-field applied in the SQUID magnetometer. ($\varphi = 70°$ is close to the hard direction of the

UNCORRECTED PROOF

magnetization). Fig. 6(a) shows: (i) the M(H) loops taken before the ZFH protocol (T = 300 K, black filled squares); (ii) after the ZFH protocol (T = 600 K, red open circles) and (iii) after the ZFC (T = 300 K, green filled triangles). As discussed in Section III-A, the M(H) loop of the as-prepared Sample B (before the ZFH protocol) is not centered due to the $K_{eff}^{NiFe/IrMn}$ anisotropy [see zoom in Fig. 6(a)]. After the ZFH protocol, the M(H) loop at 600 K is still off-center and opened but more obviously shows a strong reduction in saturation magnetization (60%). Furthermore, an additional decrease of ≈ 35% of the magnetization is recorded between the beginning and the end of the M(H) loop at 600 K. The reduction in magnetization is probably related to the increase of the Ta content in the NiFe layer as previously reported [64]. This assumption will be corroborated by RT XRR measurements of Sample B after it has been heated up to 600 K (discussed hereafter) . Along the same line, the presence of a time irreversibility effect in the hysteresis loop can be attributed to the continuation of the Ta diffusion phenomenon during the measurement. The M(H) loop, collected at 300 K after the ZFH/ZFC protocols, is completely centered, indicating that K_{EB} set in the as prepared sample by K_{eff}^{NiFe} vanished and the anomalous shift has been removed. Also, a 40% reduction in the M_S value is observed when compared to the as-prepared sample measured at 300 K (black filled squares). This is in agreement with the previously discussed in-

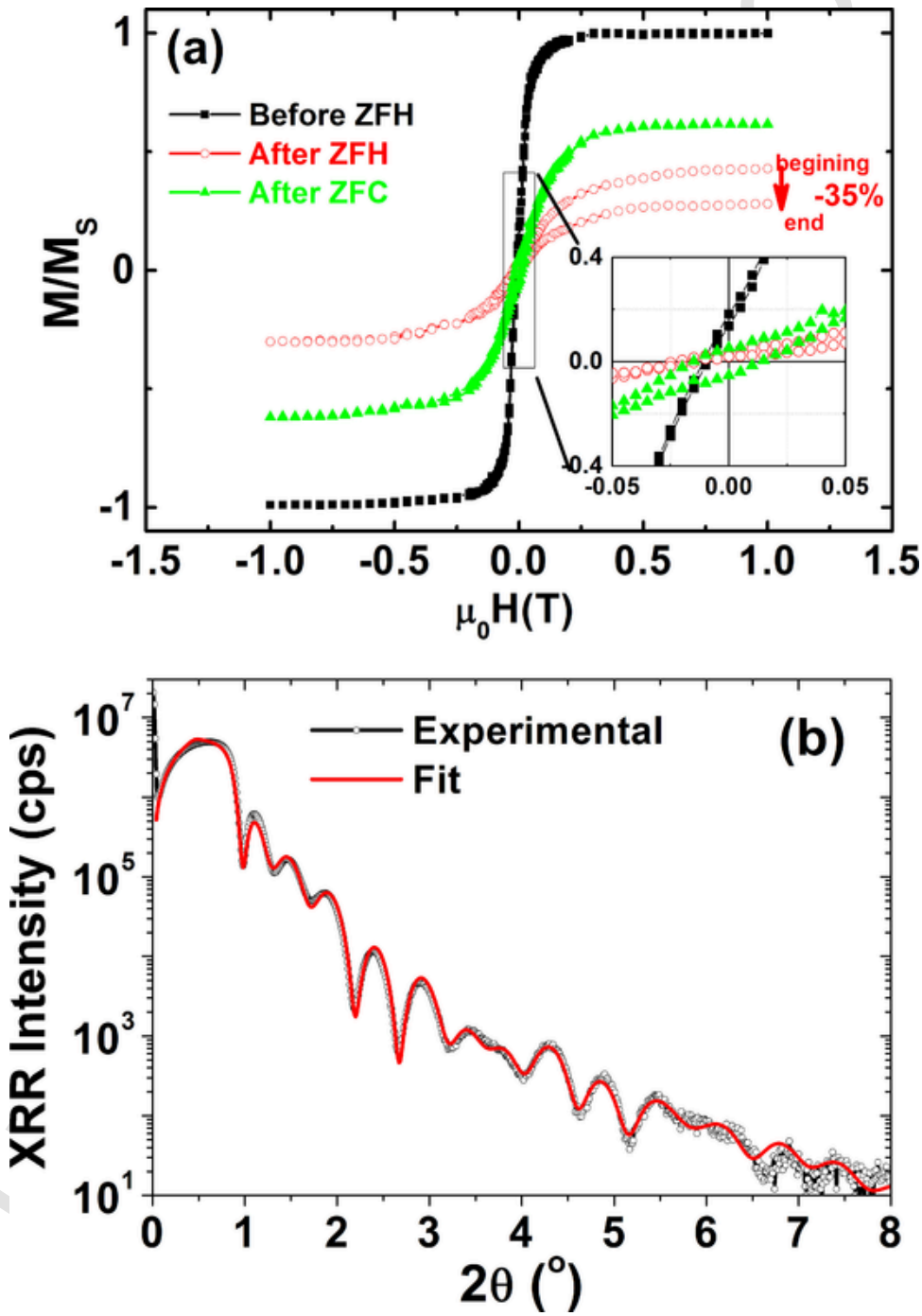

FIG. 6. (a) M(H) hysteresis loops taken before the ZFH (1/3, 300 K, black squares), after the ZFH (2/3, 600 K, red circles) and after the ZFC (3/3, 300 K, green triangles) protocols. The maximum temperature is T_{max} = 600 K, φ = 70°, and the maximum magnetic field is 1 T. The inset shows a zoom of central parts of the hysteresis loops. (b) RT XRR pattern of the Sample B after annealing at 600 K (black symbols) and the respective fitting (red line) using the Dyna code [48].

crease of the intermixing. Moreover, the third M(H) loop (green triangles) exhibits an 80% increase of the M_S value when compared with the loop obtained at 600 K (red open circles), as expected by the Brillouin curve behavior. Besides this effect, the slope of the M(H) loop has changed, turning harder to reach magnetization saturation, compared with the first 300 K M(H) loop recorded for the as-prepared Sample B (black squares). Indeed, the couple [$\chi_{max}(mT)^{-1}$, $\mu_0 H_{sat}(mT)$] reaches [2.2×10^{-2},318.0] and [9.5×10^{-3},539.6] for the as-prepared and after the ZFC procedure, respectively. The M(T) analysis revealed that the maximum temperature of setting, which does not result in damage of the interfaces, is 460 K.

In order to follow the degradation of the sample produced by the annealing process, XRR measurements were applied on the Sample B annealed at 600 K. Fig.6(b) shows the RT XRR pattern of Sample B after annealing at 600 K. A very good fit (red line) of the experimental reflectivity curve (black open circle) has been obtained and the derived parameters are given in Table IV. We checked that the sum of nominal thicknesses [t(Ta) + t(NiFe) + t(IrMn) = 3 + 3 + 8 = 14 nm] is close to fitted thicknesses [t(Ta) + t(NiFeTa) + t(NiFe) + t(IrMn) = 2.3 + 1.8 + 2.0 + 7.7 = 13.8 nm].

The XRR results confirm the extension of the alloy layer at the interface of the Ta and $Ni_{80}Fe_{20}$ layers because while the thickness of the NiFeTa layer increases by 0.9 nm, that of the NiFe layer decreases by the same amount. This can explain the 40% reduction of M_S after the application of the ZFH/ZFC protocols between 300 K and 600 K, since as already discussed NiFeTa has a M_S value lower than that for NiFe [64]. The alloying process had already been observed for thicker EB systems with 3d elements thermally annealed in this temperature range [65], however, this systematic work also brings a full comprehension of how the thermal annealing can influence the structural and magnetic properties of the Ta/NiFe interface which, consequently, intrinsically affects the global properties of this type of multilayer.

IV. Conclusion

Anomalous magnetic hysteresis loop shifts emerged in an ultrathin Si(100)/Ta/NiFe/IrMn/Ta heterostructures that were deposited in zero magnetic field using oblique incidence in a confocal magnetron sputtering setup, with the sample holder rotating at 0.5 Hz. This uncommon exchange bias field is set at the NiFe/IrMn interface by the spontaneous magnetization of the NiFe layer along an easy uniaxial anisotropy axis, which was induced by the combination of the shadowing effect due to the oblique incidence of the sputtering flux and the atomic diffusion at the Ta/$Ni_{80}Fe_{20}$ interface. Therefore, we conclude that the shift and features of the hysteresis loops depends strongly on the orientation of the applied magnetic field with respect to the direction of the easy axis of the effective anisotropy of the multilayer (the effective anisotropy includes uniaxial and unidirectional terms). The structural analysis of the as-prepared sample suggests that the NiFe/IrMn stacking has a [111] preferential orientation and confirms the existence of a NiFeTa alloy formed by the atomic diffusion at the bottom Ta/$Ni_{80}Fe_{20}$ interface as initially observed for a Ta/NiFe/Ta reference heterostructure. Thus, the ferromagnetic layer is formed by the top $Ni_{80}Fe_{20}$ sublayer (soft) and the bottom NiFeTa alloy (hard). This explains why the M(H) loops only saturate for fields reaching 0.2–0.3 T and also the higher calculated value for the uniaxial anisotropy constant of the ferromagnetic layer which favors a preferentially oriented spontaneous magnetization. The harder NiFeTa alloy makes this spontaneous magnetization sufficiently intense to pin the AF moments to the FM ones during the IrMn deposition, as soon as the AF order is established and, consequently, setting the exchange bias. The presence of such a harder NiFeTa alloy at the bottom of the NiFe layer and its impact on the exchange bias properties could only be revealed in the ultrathin dimension and would be imperceptible in thicker samples. The anomalous shift can also be removed by a thermal annealing up to about 600 K, however, a degradation of the samples occurs in this temperature range due to an enhancement of atomic diffusion at the interfaces (mostly at the bottom Ta/NiFe interface), provoking a 40% reduction of the M_S quantity. The knowledge of the structural, magnetic and thermal properties and the control of the magnetic anisotropy of this type of ultrathin films is a fundamental issue, since soft magnetic NiFe ultrathin films have often been suggested to be applied in several nanodevices.

TABLE IV
Fit parameters (thickness t with t_n as the nominal one, roughness σ and density ρ) extracted from the XRR pattern of the Sample B annealed at 600 K. Uncertainties are in the parenthesis, and the expected density is given in square brackets. The asterisk indicates the nominal thickness is related to the deposited Ta layer, but the corresponding parameters obtained from the fit are associated with the completely oxidized $Ta_{29}O_{71}$ layer.

Sample B annealed at 600 K				
	t_n (nm)	t (nm)	σ (nm)	ρ (g/cm^3)
Ta* - $Ta_{29}O_{71}$	1.0*	3.8(1.0)	0.9(0.2)	7.6(1.1) [8.37]
$Ir_{20}Mn_{80}$	8.0	7.7(0.5)	0.3(0.1)	10.3(0.1) [10.28]
$Ni_{80}Fe_{20}$	*3.0*	2.0(0.5)	0.4(0.1)	8.0(0.8) [8.69]
$Ni_{40}Fe_{10}Ta_{50}$		1.8(0.4)	0.5(0.2)	12.6(1.0) [13.17]
Ta(buffer)	3.0	2.3(0.5)	0.5(0.2)	15.7(1.5) [16.05]
Si(100)			0.3(0.1)	2.33(0.02) [2.33]

Declaration of Competing Interest

The authors declare that they have no known competing financial interests or personal relationships that could have appeared to influence the work reported in this paper.

Acknowledgements

The authors of this paper are immensely grateful for the financial support provided by the following Brazilian agencies: FAPES, CNPq, CAPES and UFES. We also thank Institute Néel/CNRS at France for providing us the infrastructure for most experiments. The authors acknowledge Danny Mannix for a critical reading of the manuscript.

References

[1] C. Chappert, A. Fert, F.N. V.an Dau, The emergence of spin electronics in data storage, Nat. Mater. 6 (2007) 813–823, https://doi.org/10.1038/nmat2024.
[2] S.D. B.ader, S.S. P.arkin, Spintronics, Annu. Rev. Condens. Matter Phys. 1 (2010) 71–88, https://doi.org/10.1146/annurev-conmatphys-070909-104123.
[3] A. Hirohata, Y. Nakatan. K.Yamada, I. Prejbeanu, B. Diény, P. Pirro, B. Hillebrands, Review on spintronics: Principles and device applications, J. Magn. Magn. Mater. 509 (2020) 166711, https://doi.org/10.1016/j.jmmm.2020.166711.
[4] J. McCord, C. Hamann, R. Schäfer, L. Schultz, R. Mattheis, Nonlinear exchange coupling and magnetic domain asymmetry in ferromagnetic/IrMn thin films, Phys. Rev. B 78 (2008) 094419, https://doi.org/10.1103/PhysRevB.78.094419.
[5] E. Jiménez, J. Camarero, J. Sort, J. Nogués, N. Mikuszeit, J.M. G.arcía-Martín, A. Hoffmann, B. Dieny, R. Miranda, Emergence of noncollinear anisotropies from interfacial magnetic frustration in exchange-bias systems, Phys. Rev. B 80 (2009) 014415, https://doi.org/10.1103/PhysRevB.80.014415.
[6] D. Maryenko, M. Kawamura, A. Ernst, V.K. D.ugaev, E. Ya. Sherman, M. Kriener, M.S. B.ahramy, Y. Kozuka, M. Kawasaki, Interplay of spin–orbit coupling and Coulomb interaction in ZnO-based electron system, Nat. Commun. 12 (2021) 3180, https://doi.org/10.1038/s41467-021-23483-4.
[7] S. Eisman. Jörg, Peter Banzer, Martin Neugebauer, Spin-orbit coupling affecting the evolution of transverse spin, Phys. Rev. Research 1 (2019) 033143, https://doi.org/10.1103/PhysRevResearch.1.033143.
[8] D. Wu, Z. Zhang, L. Li, Z. Zhang, H.B. Z.hao, J. Wang, B. Ma, Q.Y. J.in, Perpendicular magnetic anisotropy and magnetization dynamics in oxidized CoFeAl films, Sci. Rep. 5 (2015) 12352, https://doi.org/10.1038/srep12352.
[9] A.S. S.amardak, A.V. D.avydenko, A.G. K.olesnikov, et al., Enhancement of perpendicular magnetic anisotropy and Dzyaloshinskii–Moriya interaction in thin ferromagnetic films by atomic-scale modulation of interfaces, NPG Asia Mater 12 (2020) 51, https://doi.org/10.1038/s41427-020-0232-9.
[10] A. Barranco, A. Borras, A.R. G.onzalez-Elipe, A. Palmero, Perspectives on oblique angle deposition of thin films: From fundamental to devices, Prog. Mater. Sci. 76 (2016) 59–153, https://doi.org/10.1016/j.pmatsci.2015.06.003.
[11] D. Sander, The correlation between mechanical stress and magnetic anisotropy in

UNCORRECTED PROOF

ultrathin films, Rep. Prog. Phys. 62 (1999) 809–858, https://doi.org/10.1088/0034-4885/62/5/204.
[12] D. Sander, The magnetic anisotropy and spin reorientation of nanostructures and nanoscale films, J. Phys.: Condens. Matter 16 (2004) R603, https://doi.org/10.1088/0953-8984/16/20/R01.
[13] T. Blachowicz, A. Ehrmann, Exchange Bias in Thin Films—An Update, Coat 11 (2021) 122, https://doi.org/10.3390/coatings.11020122.
[14] L.E. F.ernandez-Outon, M.S. A.raújo Filho, R.E. A.raújo, J.D. A.rdisson, W.A.A. Macedo, Setting temperature effect in polycrystalline exchange-biased IrMn/CoFe bilayers, J. Appl. Phys. 113 (2013) 17D704, https://doi.org/10.1063/1.4795211.
[15] F. Offi, W. Kuch, L.I. Chelaru, M. Kotsugi, J. Kirschner, Local exchange bias observed by photoemission microscopy, J. Magn. Magn. Mater. 261 (2003) L1–L6, https://doi.org/10.1016/S0304-8853(02)01481-6.
[16] A.C. K.rohling, T.E.P. Bueno, V.P. N.ascimento, C. Larica, K. Krambrock, D. Menzel, F.J. L.itterst, E.C. P.assamani, Spin valve heterostructures built using the shadowing effect: Setting NiFe and Co magnetization directions for non-collinear couplings, Appl. Phys. Lett. 111 (2017) 262404, https://doi.org/10.1063/1.5003220.
[17] V.P. Nascimento, E.C. Passamani, A.D. Alvarenga, A. Biondo, F. Pelegrini, E. Baggio Saitovitch, Bottom and top AF/FM interfaces of NiFe/FeMn/NiFe trilayers, Appl. Surf. Sci. 254 (2008) 2114–2119, https://doi.org/10.1016/j.apsusc.2007.08.065.
[18] V.P. Nascimento, E.C. Passamani, A.D. Alvarenga, F. Pelegrini, A. Biondo, E. Baggio Saitovitch, Influence of the roughness on the exchange bias effect of NiFe/FeMn/NiFe trilayers, J. Magn. Magn. Mater. 320 (2008) e272–e274, https://doi.org/10.1016/j.jmmm.2008.02.059.
[19] V.P. Nascimento, I.L.C. Merino, E.C. Passamani, W. Alayo, M. Tafur, F. Pelegrini, R. Magalhães-Paniago, A.D. Alvarenga, E.B. Saitovitch, Clarifying roughness and atomic diffusion contributions to the interface broadening in exchange-biased NiFe/FeMn/NiFe heterostructures, Thin Solid Films 542 (2013) 360–367, https://doi.org/10.1016/j.tsf.2013.06.097.
[20] I.L. C.astro, V.P. N.ascimento, E.C. P.assamani, A.Y. T.akeuchi, C. Larica, M. Tafur, F. Pelegrini, The role of the (111) texture on the exchange bias and interlayer coupling effects observed in sputtered NiFe/IrMn/Co trilayers, J. Appl. Phys. 113 (2013) 203903, https://doi.org/10.1063/1.4804671.
[21] R. Jérome, T. Valet, P. Galtier, Correlation Between Magnetic and Structural Properties of $Ni_{80}Fe_{20}$ Sputtered Thin Films Deposited on Cr and Ta Buffer Layers, IEEE Trans. Magn. 30 (1994) 4878–4880, https://doi.org/10.1109/20.334252.
[22] M.A. M.ilyaev, L.I. N.aumova, V.V. P.roglyado, T.P. K.rinitsina, I.S. B.annikova, A.M. B.urkhanov, V.V. U.stinov, Degree of Perfection of the <111> Texture and the Hysteresis of Magnetoresistance in MnIr-Based Top Spin Valves, Phys. Met. Metallogr. 114 (2013) 383–389, https://doi.org/10.1134/S0031918X13050050.
[23] Yong-Jin Song, Seung-Ki Joo, Magnetoresistance and magnetic anisotropy of permalloy based multilayers, IEEE Trans. Magn. 32 (1996) 4788–4790, https://doi.org/10.1109/20.539152.
[24] T.P. B.ertelli, T.E.P. Bueno, A.C. K.rohling, B.C. S.ilva, R.L. R.odríguez-Suárez, V.P. N.ascimento, R. Paniago, K. Krambrock, C. Larica, E.C. Passamani, Magnetic anisotropy of Co thin films: Playing with the shadowing effect, magnetic field and substrate spinning, J. Magn. Magn. Mater. 426 (2017) 636–640, https://doi.org/10.1016/j.jmmm.2016.10.157.
[25] A.C. K.rohling, C.H. v.erbeno, T.E.P. Bueno, V.P. N.ascimento, K. Krambrock, F.J. L.itterst, E.C. P.assamani, The influence of Cu spacer morphology in Cu/Py/Cu/Co/IrMn spin valves with induced non-collinear spin structures, J. Magn. Magn. Mater. 512 (2020) 166985, https://doi.org/10.1016/j.jmmm.2020.166985.
[26] N. Chowdhury, S. Bedanta, Controlling the anisotropy and domain structure with oblique deposition and substrate rotation, AIP Adv 4 (2014) 027104, https://doi.org/10.1063/1.4865248.
[27] B.D. C.ullity, C.D. G.raham, Introduction to Magnetic Materials, Wiley-IEEE Press, New Jersey, 2008.
[28] C.A.F. Vaz, J.A.C. Bland, G. Lauhoff, Magnetism in ultrathin film structures, Rep. Prog. Phys. 71 (2008) 056501, https://doi.org/10.1088/0034-4885/71/5/056501.
[29] M. Gibertini, M. Koperski, A.F. M.orpurgo, K.S. N.ovoselov, Magnetic 2D materials and heterostructures, Nat. Nanotechnol. 14 (2019) 408–419, https://doi.org/10.1038/s41565-019-0438-6.
[30] B. Heinrich, J.F. C.ochran, Ultrathin metallic magnetic films: magnetic anisotropies and exchange interactions, Adv. Phys. 42 (1993) 523–639, https://doi.org/10.1080/00018739300101524.
[31] D.L. M.ills, Surface anisotropy and surface spin canting in the semi-infinite ferromagnet, Phys. Rev. B 39 (1989) 12306–12307, https://doi.org/10.1103/PhysRevB.39.12306.
[32] R.C. O.'Handley, J.P. W.oods, Static magnetization direction under perpendicular surface anisotropy, Phys. Rev. B 42 (1990) 6568–6573, https://doi.org/10.1103/PhysRevB.42.6568.
[33] A. Thiaville, A. Fert, Twisted spin configurations in thin magnetic layers with interface anisotropy, J. Magn. Magn. Mater. 113 (1992) 161–172, https://doi.org/10.1016/0304-8853(92)91263-S.
[34] R.M. B.ozorth, Ferromagnetism, John Wiley & Sons, Inc., Hoboken, NewJersey, 2003.
[35] I. Hashim I, H.S. J.oo, H.A. A.twater, Structural and magnetic properties of the epitaxial Ni80Fe20 thin films on Cu/Si, Surf. Rev. Lett. 2 (1995) 427–437, https://doi.org/10.1142/S0218625X95000388.
[36] I. Hashim, H.A. A.twater, In situ magnetic and structural analysis of epitaxial Ni80Fe20 thin films for spin-valve heterostructures, J. Appl. Phys. 75 (1994) 6516–6518, https://doi.org/10.1063/1.356933.
[37] K. Hoshino, R. Nakatani, H. Hoshiya, Y. Sugita, S. Tsunashima, Exchange Coupling between Antiferromagnetic Mn–Ir and Ferromagnetic Ni–Fe Layers, J Appl. Phys. 35 (1997) 607–612, https://doi.org/10.1143/JJAP.35.607.
[38] A.J. D.evasahayam, P.J. S.ides, M.H. K.ryder, Magnetic, temperature, and corrosion properties of the NiFe/IrMn exchange couple, J. Appl. Phys. 83 (1998) 7216, https://doi.org/10.1063/1.367550.
[39] I.O. D.zhun, G.V. B.abaytsev, N.G. C.hechenin, C.A. G.ritsenko, Valeria V.Rodionova, FMR investigations of exchange biased NiFe/IrMn/NiFe trilayers with high and low Ni relative content, J. Magn. Magn. Mater. 470 (2019) 151–155, https://doi.org/10.1016/j.jmmm.2017.11.028.
[40] X.Y. L.ang, W.T. Z.heng, Q. Jiang, Dependence of the blocking temperature in exchange biased ferromagnetic/antiferromagnetic bilayers on the thickness of the antiferromagnetic layer, Nanotechnol 18 (2007) 155701, https://doi.org/10.1088/0957-4484/18/15/155701.
[41] A. Kohn, A. Kovács, R. Fan, G.J. M.cIntyre, R.C.C. Ward, J.P. G.off, The antiferromagnetic structures of IrMn3 and their influence on exchange-bias, Sci. Rep. 3 (2013) 2412, https://doi.org/10.1038/srep02412.
[42] P. Yu, X.F. J.in, J. Kudrnovský, D.S. W.ang, P. Bruno, Curie temperatures of fcc and bcc nickel and permalloy: Supercell and Green's function methods, Phys. Rev. B 77 (2008) 054431, https://doi.org/10.1103/PhysRevB.77.054431.
[43] J. van Driel, F.R. d.e Boer, K.-M.H. Lenssen, R. Coehoorn, Exchange biasing by Ir19Mn81: Dependence on temperature, microstructure and antiferromagnetic layer thickness, J. Appl. Phys. 88 (2000) 975, https://doi.org/10.1063/1.373764.
[44] S. Queste, S. Dubourg, O. Acher, J.-.C. Soret, K.-.U. Barholze, R. Mattheis, Microwave permeability study for antiferromagnet thickness dependence on exchange bias field in NiFe/lrMn layers, J. Magn.Magn. Mater. 288 (2005) 60–65, https://doi.org/10.1016/j.jmmm.2004.08.017.
[45] T. Pokhil, S. Mao, E.A. M.ack, Study of exchange anisotropy in NiFe/NiMn and NiFe/IrMn exchange coupled films, J. Appl. Phys. 85 (1999) 4916, https://doi.org/10.1063/1.369141.
[46] Yong-Goo Yoo, Seong-Gi Min, Ho-Jun Ryu, Nam-Seok Park, Seong-Cho Yu, Angular and NiFe thickness dependence of exchange bias in IrMn/NiFe/IrMn thin film, J. Magn. Magn. Mater. 303 (2006) e188–e191, https://doi.org/10.1016/j.jmmm.2006.01.051.
[47] Y. Tserkovnyak, A. Brataas, G.E.W. Bauer, Spin pumping and magnetization dynamics in metallic multilayers, Phys. Rev. B. 66 (2002) 224403, https://doi.org/10.1103/PhysRevB.66.224403.
[48] Y. Tserkovnyak, A. Brataas, G.E.W. Bauer, Enhanced Gilbert Damping in Thin Ferromagnetic Films, Phys. Rev. Lett. 88 (2002) 117601, https://doi.org/10.1103/PhysRevLett.88.117601.
[49] L. Frangou, S. Oyarzún, S. Auffret, L. Vila, S. Gambarelli, V. Baltz, Enhanced Spin Pumping Efficiency in Antiferromagnetic IrMn Thin Films around the Magnetic Phase Transition, Phys. Rev. Lett. 116 (2016) 077203, https://doi.org/10.1103/PhysRevLett.116.077203.
[50] O. Gladii, L. Frangou, G. Forestier, R.L. S.eeger, S. Auffret, I. Joumard, M. Rubio-Roy, S. Gambarelli, V. Baltz, Unraveling the influence of electronic and magnonic spin-current injection near the magnetic ordering transition of IrMn metallic antiferromagnets, Phys. Rev. B. 98 (2018) 094422, https://doi.org/10.1103/PhysRevB.98.094422.
[51] M. Elzo, E. Jal, O. Bunau, S. Grenier, Y. Joly, A.Y. Ramos, H.C.N. Tolentino, J.M. T.onnerre, N. Jaouen, X-ray resonant magnetic reflectivity of stratified magnetic structures:Eigenwave formalism and application to a W/Fe/W trilayer, J. Magn. Magn. Mater. 324 (2012) 105–112, https://doi.org/10.1016/j.jmmm.2011.07.019.
[52] J. Colin, G. Abadias, A. Michel, C. Jaouen, On the origin of the metastableb-Ta phase stabilization in tantalum sputtered thin films, Acta Mater 126 (2012) 481–493, https://doi.org/10.1016/j.actamat.2016.12.030.
[53] M. Khanuja, H. Sharma, B.R. M.ehta, S.M. S.hivaprasad, XPS depth-profile of the suboxide distribution at the native oxide/Ta interface, J. Electron Spectrosc. Relat. Phenom. 169 (2009) 41–45, https://doi.org/10.1016/j.elspec.2008.10.004.
[54] Ke Wang, Zhi Liu, Tirma Herranz Cruz, Miquel Salmeron, Hong Liang, In Situ Spectroscopic Observation of Activation and Transformation of Tantalum Suboxides, J. Phys. Chem. A 114 (2010) 2489–2497, https://doi.org/10.1021/jp910964s.
[55] A.V. K.orshunov, A.V. P.ustovalov, T.P. M.orozova, D.O. P.erevezentseva, Oxidation of Fine Tantalum Particles: Metastable Intermediates and Multistep Kinetics, Oxid. Met. 93 (2020) 301–328, https://doi.org/10.1007/s11085-020-09957-8, 2020.
[56] S. Lecuyer, A. Quemerais, G. Jezequel, Composition of natural oxide films on polycrystalline tantalum using XPS electron take-off angle experiments, Surf. Interface Anal. 18 (1992) 257–261, https://doi.org/10.1002/sia.740180403.
[57] A. Moskaltsova, J. Krieft, .. Graulich, T. Matalla-Wagner, Kuschel T, Impact of the magnetic proximity effect in Pt on the total magnetic moment of Pt/Co/Ta trilayers studied by x-ray resonant magnetic reflectivity, AIP Adv 10 (2020) 015154, https://doi.org/10.1063/1.5130031.
[58] J.M. S.anz, S. Hofmann, Auger electron spectroscopy and X-ray photoelectron spectroscopy studies of the oxidation of polycrystalline tantalum and niobium at room temperature and low oxygen pressures, J. Less Common Met. 92 (1983) 317–327, https://doi.org/10.1016/0022-5088(83)90498-8.
[59] Kuo-Hao Chang, Stochastic Nelder–Mead simplex method – A new globally convergent direct search method for simulation optimization, Eur. J. Oper. Res. 220 (2012) 684–694, https://doi.org/10.1007/s11664-016-4613-3.10.1016/j.ejor.2012.02.028.
[60] C.T. C.hantler, Detailed Tabulation of Atomic Form Factors, Photoelectric Absorption and Scattering Cross Section, and Mass Attenuation Coefficients in the Vicinity of Absorption Edges in the Soft X-Ray (Z = 30-36, Z = 60-89, E = 0.1 keV-10 keV), Addressing Convergence Issues of Earlier Work, J. Phys. Chem. Ref.

UNCORRECTED PROOF

Data 29 (2000) 597–1048.
[61] C.T. C.hantler, Theoretical Form Factor, Attenuation and Scattering Tabulation for Z = 1-92 from E = 1-10 eV to E = 0.4-1.0 MeV, J. Phys. Chem. Ref. Data 24 (1995) 71–643.
[62] N.N. P.huoc, C.K. O.ng, Comparative Study of Thermal Stability of NiFe and NiFeTa Thin Films Grown by Cosputtering Technique, J. Electron. Mater. 45 (2016) 4061–4066, https://doi.org/10.1007/s11664-016-4613-3.
[63] N.N. P.huoc, C.K. O.ng, Strain-driven fractional spontaneous exchange bias in ferromagnetic/antiferromagnetic thin films with composition-graded ferromagnetic layer, J. Appl. Phys. 115 (2014) 143901, https://doi.org/10.1063/1.4871284.
[64] M. Kitada, K. Yamamoto, Soft magnetic properties of NiFeTa thin films for biasing film applications in magnetoresistive elements, J. Mater. Sci.: Mater. Electron. 7 (1996) 447–449, https://doi.org/10.1007/BF00180784.
[65] O. Grady, K. Fernandez-Outon, L.E.G. Vallejo-Fernandez, A new paradigm for exchange bias in polycrystalline thin films, J. Magn. Magn. Mater. 322 (2010) 883–899, https://doi.org/10.1016/j.jmmm.2009.12.011.

UNCORRECTED PROOF